



Universiteit
Leiden
The Netherlands

GOALS-JWST: tracing AGN feedback on the star-forming interstellar medium in NGC 7469

Lai, T.S.-Y.; Armus, L.; U, V.; Díaz-Santos, T.; Larson, K.L.; Evans, A.; ... ; Surace, J.

Citation

Lai, T. S. -Y., Armus, L., U., V., Díaz-Santos, T., Larson, K. L., Evans, A., ... Surace, J. (2022). GOALS-JWST: tracing AGN feedback on the star-forming interstellar medium in NGC 7469. *Astrophysical Journal Letters*, 941(2), L36. doi:10.3847/2041-8213/ac9ebf

Version: Publisher's Version
License: [Creative Commons CC BY 4.0 license](#)
Downloaded from: <https://hdl.handle.net/1887/3561913>

Note: To cite this publication please use the final published version (if applicable).



GOALS-JWST: Tracing AGN Feedback on the Star-forming Interstellar Medium in NGC 7469

Thomas S.-Y. Lai (賴劭愉)¹, Lee Armus¹, Vivian U², Tanio Díaz-Santos^{3,4}, Kirsten L. Larson⁵, Aaron Evans^{6,7}, Matthew A. Malkan⁸, Philip Appleton¹, Jeff Rich⁹, Francisco Müller-Sánchez¹⁰, Hanae Inami¹¹, Thomas Bohn¹¹, Jed McKinney¹², Luke Finnerty⁸, David R. Law¹³, Sean T. Linden¹⁴, Anne M. Medling^{15,16}, George C. Privon^{6,17}, Yiqing Song^{6,7}, Sabrina Stierwalt¹⁸, Paul P. van der Werf¹⁹, Loreto Barcos-Muñoz^{6,7}, J. D. T. Smith²⁰, Aditya Togi²¹, Susanne Aalto²², Torsten Böker²³, Vassilis Charmandaris^{3,4,24}, Justin Howell¹, Kazushi Iwasawa^{25,26}, Francisca Kemper^{27,28,29}, Joseph M. Mazzarella¹, Eric J. Murphy⁶, Michael J. I. Brown³⁰, Christopher C. Hayward³¹, Jason Marshall³², David Sanders³³, and Jason Surace¹

¹ IPAC, California Institute of Technology, 1200 East California Boulevard, Pasadena, CA 91125, USA; ThomasLai.astro@gmail.com

² Department of Physics and Astronomy, 4129 Frederick Reines Hall, University of California, Irvine, CA 92697, USA

³ Institute of Astrophysics, Foundation for Research and Technology-Hellas (FORTH), Heraklion, 70013, Greece

⁴ School of Sciences, European University Cyprus, Diogenes street, Engomi, 1516 Nicosia, Cyprus

⁵ AURA for the European Space Agency (ESA), Space Telescope Science Institute, 3700 San Martin Drive, Baltimore, MD 21218, USA

⁶ National Radio Astronomy Observatory, 520 Edgemont Road, Charlottesville, VA, 22903, USA

⁷ Department of Astronomy, University of Virginia, 530 McCormick Road, Charlottesville, VA 22903, USA

⁸ Department of Physics & Astronomy, 430 Portola Plaza, University of California, Los Angeles, CA 90095, USA

⁹ The Observatories of the Carnegie Institution for Science, 813 Santa Barbara Street, Pasadena, CA 91101, USA

¹⁰ Department of Physics and Materials Science, University of Memphis, 3720 Alumni Avenue, Memphis, TN 38152, USA

¹¹ Hiroshima Astrophysical Science Center, Hiroshima University, 1-3-1 Kagamiyama, Higashi-Hiroshima, Hiroshima 739-8526, Japan

¹² Department of Astronomy, University of Massachusetts, Amherst, MA 01003, USA

¹³ Space Telescope Science Institute, 3700 San Martin Drive, Baltimore, MD 21218, USA

¹⁴ Department of Astronomy, University of Massachusetts at Amherst, Amherst, MA 01003, USA

¹⁵ Department of Physics & Astronomy and Ritter Astrophysical Research Center, University of Toledo, Toledo, OH 43606, USA

¹⁶ ARC Centre of Excellence for All Sky Astrophysics in 3 Dimensions (ASTRO 3D), Australia

¹⁷ Department of Astronomy, University of Florida, P.O. Box 112055, Gainesville, FL 32611, USA

¹⁸ Physics Department, 1600 Campus Road, Occidental College, Los Angeles, CA 90041, USA

¹⁹ Leiden Observatory, Leiden University, PO Box 9513, 2300 RA Leiden, The Netherlands

²⁰ Ritter Astrophysical Research Center, University of Toledo, Toledo, OH 43606, USA

²¹ Department of Physics, Texas State University, 601 University Drive, San Marcos, TX 78666, USA

²² Department of Space, Earth and Environment, Chalmers University of Technology, SE-412 96 Gothenburg, Sweden

²³ European Space Agency, Space Telescope Science Institute, Baltimore, MD 21218, USA

²⁴ Department of Physics, University of Crete, Heraklion, 71003, Greece

²⁵ Institut de Ciències del Cosmos (ICCUB), Universitat de Barcelona (IEEC-UB), Martí i Franquès, 1, E-08028 Barcelona, Spain

²⁶ ICREA, Pg. Lluís Companys 23, E-08010 Barcelona, Spain

²⁷ Institut de Ciències de l'Espai (ICE, CSIC), Can Magrans, s/n, E-08193 Bellaterra, Barcelona, Spain

²⁸ ICREA, Pg. Lluís Companys 23, Barcelona, Spain

²⁹ Institut d'Estudis Espacials de Catalunya (IEEC), E-08034 Barcelona, Spain

³⁰ School of Physics and Astronomy, Monash University, Clayton, VIC 3800, Australia

³¹ Center for Computational Astrophysics, Flatiron Institute, 162 Fifth Avenue, New York, NY 10010, USA

³² Glendale Community College, 1500 N. Verdugo Road, Glendale, CA 91208, USA

³³ Institute for Astronomy, University of Hawaii, 2680 Woodlawn Drive, Honolulu, HI 96822, USA

Received 2022 September 14; revised 2022 October 19; accepted 2022 October 31; published 2022 December 23

Abstract

We present James Webb Space Telescope (JWST) Mid-Infrared Instrument (MIRI) integral-field spectroscopy of the nearby merging, luminous infrared galaxy, NGC 7469. This galaxy hosts a Seyfert type-1.5 nucleus, a highly ionized outflow, and a bright, circumnuclear star-forming ring, making it an ideal target to study active galactic nucleus (AGN) feedback in the local universe. We take advantage of the high spatial/spectral resolution of JWST/MIRI to isolate the star-forming regions surrounding the central active nucleus and study the properties of the dust and warm molecular gas on ~ 100 pc scales. The starburst ring exhibits prominent polycyclic aromatic hydrocarbon (PAH) emission, with grain sizes and ionization states varying by only $\sim 30\%$, and a total star formation rate of $10\text{--}30 M_{\odot} \text{ yr}^{-1}$ derived from fine structure and recombination emission lines. Using pure rotational lines of H_2 we detect $1.2 \times 10^7 M_{\odot}$ of warm molecular gas at a temperature higher than 200 K in the ring. All PAH bands get significantly weaker toward the central source, where larger and possibly more ionized grains dominate the emission, likely the result of the ionizing radiation and/or the fast wind emerging from the AGN. The small grains and warm molecular gas in the bright regions of the ring however display properties consistent with normal star-forming regions. These observations highlight the power of JWST to probe the inner regions of dusty, rapidly



Original content from this work may be used under the terms of the [Creative Commons Attribution 4.0 licence](https://creativecommons.org/licenses/by/4.0/). Any further distribution of this work must maintain attribution to the author(s) and the title of the work, journal citation and DOI.

evolving galaxies for signatures of feedback and inform models that seek to explain the coevolution of supermassive black holes and their hosts.

Unified Astronomy Thesaurus concepts: Seyfert galaxies (1447); Active galactic nuclei (16); Polycyclic aromatic hydrocarbons (1280); Starburst galaxies (1570); Luminous infrared galaxies (946)

1. Introduction

Probing the dust and gas in the interstellar medium (ISM) of merging luminous infrared galaxies (LIRGs; $L_{\text{IR}} = 10^{11-12} L_{\odot}$) is fundamental for understanding the growth of central supermassive black holes (see the review by Alexander & Hickox 2012) and the coevolution of black holes and galaxies, manifested, for example, in the black hole mass to stellar bulge mass relation (Magorrian et al. 1998). There is evidence that feedback from active galactic nuclei (AGNs) may strongly influence the properties of the ISM and hence star formation activity in their host galaxies (Howell et al. 2007). Infrared observations provide direct probes of the interplay between starbursts and AGNs, enabling us to study physical conditions of the multiphase dust and gas in even highly obscured sources (Sajina et al. 2022). In particular, Spitzer was successful in furthering our understanding of the powering sources and ISM conditions within LIRGs over a wide range of epochs, from cosmic noon to the present (see Armus et al. 2020 for a review of discoveries with the infrared spectrograph, IRS, in particular). While Spitzer provided a huge leap forward, it was a relatively small telescope and was limited by its spatial and spectral resolution in many cases.

More AGNs are found in LIRGs than in normal galaxies (Petric et al. 2011; Alonso-Herrero et al. 2012), but their contribution to the bolometric luminosity is often small ($\sim 10\%$ or less; Díaz-Santos et al. 2017). In ultraluminous infrared galaxies (ULIRGs; $L_{\text{IR}} \geq 10^{12} L_{\odot}$), the AGN contributions can be significantly higher (e.g., Armus et al. 2004, 2007; Veilleux et al. 2009; Marshall et al. 2018). This makes LIRGs an important class of extragalactic objects that bridge the gap between relatively quiescent normal galaxies and ULIRGs and quasi-stellar objects (QSOs; Le Floch et al. 2005). The diversity of galaxy interaction stages, from nonmerging, isolated spiral galaxies to late stage mergers within the local LIRG population provides an opportunity to assess AGN growth and star formation in different environments and merger stages (see the review by U 2022).

In the near and mid-infrared, strong emission from ionized atomic gas, warm molecular gas, and dust provide a direct probe of the multiphase ISM. In particular, emission from polycyclic aromatic hydrocarbons (PAHs; e.g., Tielens 2008) in the mid-infrared from photodissociation regions (PDRs) can serve as a sensitive diagnostic of the ambient radiation field and can, in many cases, potentially serve as an accurate star formation rate (SFR) indicator (e.g., Peeters et al. 2004; Lai et al. 2020). Because the carriers of the PAH emission are fragile, they are easily destroyed in harsh radiation environments. Indeed, PAH emission is often absent or very weak in the mid-infrared spectra of low metallicity galaxies (Wu et al. 2006; Hao et al. 2009) as well as Seyfert galaxies and QSOs (Smith et al. 2007; O’Dowd et al. 2009; Diamond-Stanic & Rieke 2010), although some studies have suggested that PAHs can also be excited by AGN photons (Howell et al. 2007; Smith et al. 2007; Jensen et al. 2017). PAHs are thus sensitive to the ISM in the circumnuclear environments of galaxies with ongoing star formation and accreting black holes.

NGC 7469 (Arp 298, Mrk 1514, IRAS F23007+0836) is a LIRG ($L_{8-1000\mu\text{m}} = 10^{11.6} L_{\odot}$) located at a distance of $D_L = 70.6$ Mpc. It is classified as a Seyfert 1.5 (Landt et al. 2008) galaxy with a supermassive black hole mass of $1.1 \times 10^7 M_{\odot}$ (Peterson et al. 2014; Lu et al. 2021) and X-ray luminosity of $L_{2-10\text{keV}} = 10^{43.19} \text{ erg s}^{-1}$ (Asmus et al. 2015). NGC 7469 hosts both a rapidly accreting black hole and a circumnuclear starburst ring with a radius of ~ 500 pc (e.g., Song et al. 2021), consisting of two distinct stellar populations of young ($\sim 5-6$ Myr) and intermediate ages ($\sim 14-35$ Myr; Díaz-Santos et al. 2007; Bohn et al. 2022). A highly perturbed galaxy, IC 5283, lies ~ 26 kpc ($79''$) away in projection; interaction with this companion may have triggered the starburst and AGN activity in NGC 7469. Observations based on the Very Large Telescope (VLT)/SINFONI and VLT/MUSE have shown small and large-scale outflows in the ionized atomic gas (Müller-Sánchez et al. 2011; Robledo-Orús et al. 2021; Xu & Wang 2022) and the Atacama Large Millimeter/submillimeter Array (ALMA) observations have shown a strong enhancement in [C I] emission (Izumi et al. 2020; Nguyen et al. 2021) suggestive of AGN heating. In this Letter we use the superb spatial and spectral resolution of JWST/MIRI to trace the physical conditions of the dust and molecular gas in the starburst ring and inner ISM in NGC 7469 in the mid-infrared.

Throughout this Letter, a cosmology with $H_0 = 70 \text{ km s}^{-1} \text{ Mpc}^{-1}$, $\Omega_M = 0.30$, and $\Omega_{\Lambda} = 0.70$ is adopted. The redshift of NGC 7469 ($z = 0.01627^{34}$) corresponds to a projected physical scale of $330 \text{ pc arcsec}^{-1}$.

2. Observations and Data Reduction

As part of the Director’s Discretionary Time Early Release Science program 1328 (Co-PIs: L. Armus and A. Evans), the JWST Mid-Infrared integral-field spectroscopy observations on NGC 7469 were taken with the Mid-Infrared Instrument (MIRI; Rieke et al. 2015; Labiano et al. 2021) in medium resolution spectroscopy mode (MRS; Wells et al. 2015). MRS observations are carried out using a set of four integral-field units (channels 1–4), covering a full range of $4.9-28.1 \mu\text{m}$ with three grating settings, SHORT (A), MEDIUM (B), and LONG (C) in each channel. For each subchannel, the science exposure time was 444 s and a four-pt dither pattern was used to sample the extended star-forming ring.

We downloaded the uncalibrated science and background observations through the MAST portal. The data reduction process was done using the JWST Science Calibration Pipeline (Bushouse et al. 2022) version 1.6+. Three stages of the pipeline processing were applied, including `Detector1`, `Spec2`, and `Spec3`. Additional fringe corrections were made in both the stage 2 and stage 3 products using the prototype pipeline code. We refer the readers to our companion paper (U et al. 2022) for more details on the data processing.

³⁴ NASA/IPAC Extragalactic Database.

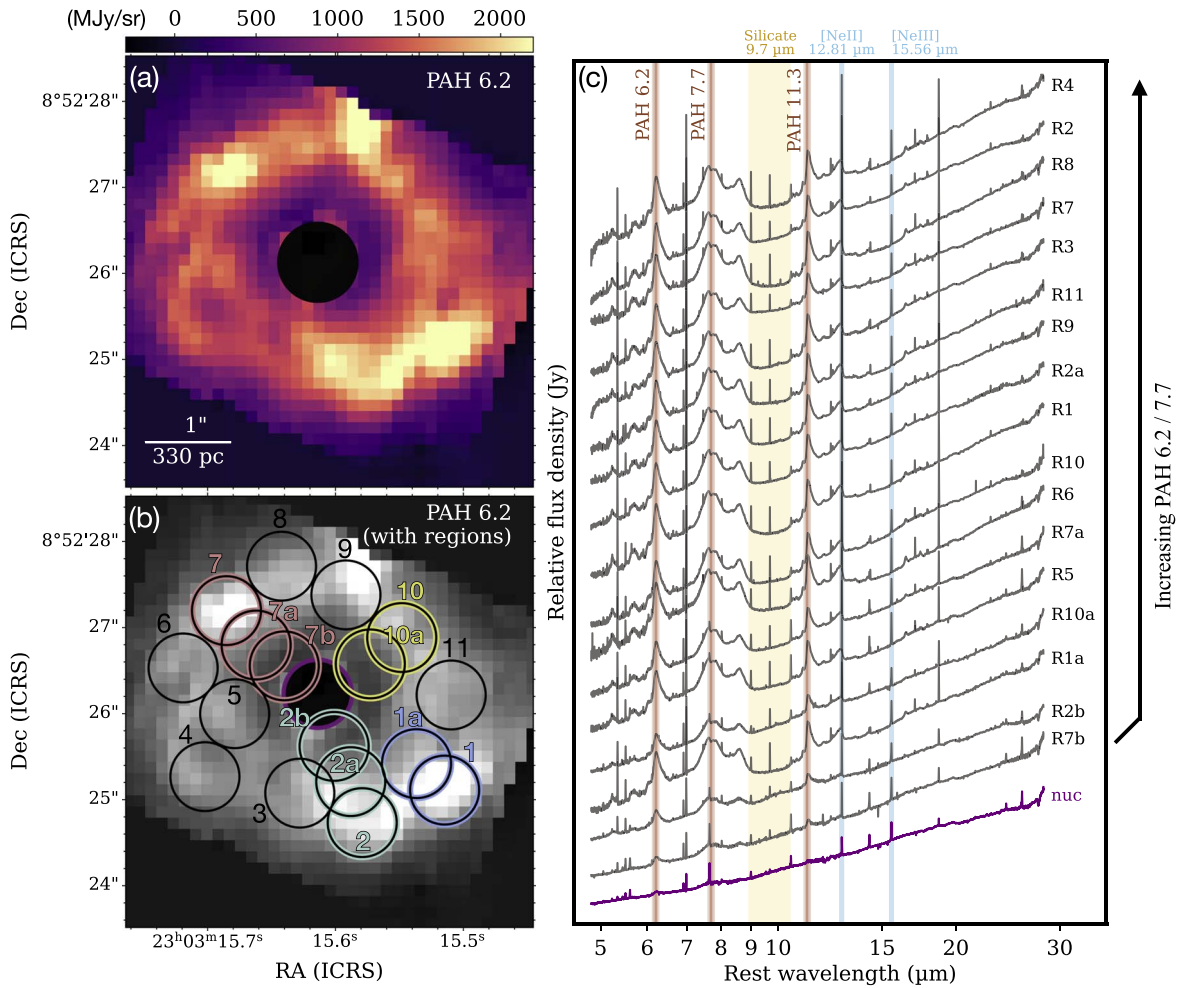


Figure 1. Extractions of the JWST/MIRI spectra in this study. (a) The $6.2\ \mu\text{m}$ polycyclic aromatic hydrocarbon (PAH) map created by applying a local continuum subtraction using the QFitsView tool (Ott 2012). (b) The same map as (a) overlaid with 17 apertures (each with a diameter of $0.8''$) used to characterize the dust and line emission of the circumnuclear ring and the inner ISM region. Regions R1–R11 cover mostly the circular ring, while regions R1a, R2a/b, R7a/b, and R10a are used to study changes of the ISM properties in the radial direction. In addition, the central black area marks the region for the nucleus extraction. (c) The nucleus spectrum is shown in purple. Other ring extracted spectra are sorted by the $6.2/7.7$ PAH ratio in ascending order from bottom to top. The main PAH features (red) and neon lines (blue) used in this study are highlighted together with the silicate absorption (yellow), which is mainly used for constraining the extinction level in spectral decomposition.

3. Results

The field of view of JWST MIRI MRS fully covers the NGC 7469 circumnuclear ring, enabling us to study the star formation and the properties of the dust and gas in the mid-infrared at unprecedented spatial and spectral resolution.

The NGC 7469 starburst ring is resolved, and is bright in PAH emission (see Figure 1(a)). The 6.2 , 7.7 , and $11.3\ \mu\text{m}$ PAH emissions, which are sensitive to the size and ionization state of the small dust grains, exhibit a complex distribution around the ring, and a variation in surface brightness by a factor of ~ 3 in the three PAH maps (here we show the $6.2\ \mu\text{m}$ map only). Since the mid-infrared spectra are rich in multiple tracers of the dust, atomic, and molecular gas, it is necessary to perform detailed fits to the data to extract key properties of the star-forming ISM.

To allow for detailed spatially resolved spectral analysis, we placed 17 apertures around the ring at radii of $\sim 0.8\text{--}1.5''$ (260–500 pc) from the center together with an extraction centered on the AGN. While a spaxel-based analysis might provide the highest resolution and take full advantage of the MIRI integral field unit (IFU) data, a proper analysis requires convolving

the cube to a common resolution and a careful spectral decomposition, taking into account both the spectral and spatial dependencies. These advanced functionalities are currently under development for JWST (T. Díaz-Santos et al. 2022, in preparation). For the purposes of this initial analysis of the MIRI/MRS data, in this study we focus on a robust aperture-based analysis. The placement of the spectral extraction apertures in the ring are determined using the continuum-subtracted $6.2\ \mu\text{m}$ PAH image created from the MIRI MRS cube (see Figure 1(a)). Among these 17 spectral regions in Figure 1(b), we first placed nonoverlapping regions R1–R11. Regions R1, R2, R7, and R9 are associated with the areas of brightest PAH emission (R9 cannot be centered at the peak of the emission due to missing cube segments in channel 1), with R1 being the brightest, followed closely by R7. Other apertures are placed throughout the ring to sample the full range of azimuth and surface brightness. Six additional regions, R1a, R2a/b, R7a/b, and R10a, are included for the purpose of studying the variations along the radial direction, on the inner edge of the ring and toward the Seyfert nucleus. Unlike the regions in the ring, these additional inner ring apertures can overlap. We note that our nuclear spectrum is not the same as that presented in

Armus et al. (2022), which is obtained using a smaller, cone extraction meant to isolate the gas in the immediate vicinity of the AGN.

The sizes of the spectral extraction apertures are all fixed, with a diameter of $0''.8$ that is equivalent to ~ 2 times the FWHM of the point-spread function (PSF) at $12\ \mu\text{m}$, where the longest wavelength PAH feature (PAH $11.3\ \mu\text{m}$) studied in this Letter is located. We extract the spectra using a cylinder extraction (a fixed aperture size) rather than an expanding cone (a varying aperture size to account for changes in angular resolution) because the clumps in the ring are resolved and surrounded by diffuse light. The extracted spectra are presented in Figure 1(c), sorted in order of increasing PAH 6.2/7.7 ratio. These spectra are aperture corrected based on the correction calculated using the MRS PSF models from WebbPSF (Oschmann et al. 2014).

3.1. Dust Properties in the Star-forming Ring and Nucleus of NGC 7469

To study the variations of PAH properties around the ring, we fit each extracted spectrum with a modified version of the continuum and feature extraction *CAFE* software developed by Marshall et al. (2007) for Spitzer/IRS, recently updated for JWST (see Díaz-Santos et al. 2022, in preparation). *CAFE* simultaneously fits the PAH features, the dust continuum, the silicate absorption, and the narrow fine structure atomic and molecular gas emission lines.

CAFE was originally developed to fit *Spitzer* low-resolution IRS spectra, with a resolving power of $R \sim 120$. The MIRI/MRS data have much higher spectral resolving power, $R \sim 1500\text{--}3500$, revealing not only the spectral profiles of the atomic and molecular emission lines, but also additional red components in the PAH complexes at 6.2 and $11.3\ \mu\text{m}$. To fully capture the asymmetric nature of the main PAH features, two additional Drude profiles centered at 6.27 and $11.36\ \mu\text{m}$ were included in the fits, based on the profiles reported in the Infrared Space Observatory-Short Wavelength Spectrometer (ISO-SWS) spectra (Verstraete et al. 2001). The capability of *CAFE* to fit the mid-infrared spectra from 5 to $28\ \mu\text{m}$ even at the high resolving power of MIRI/MRS is demonstrated in Figure 2(a), where the full range fit to the R1 spectrum is shown. The extinction curve, which is mainly constrained by the $9.7\ \mu\text{m}$ silicate absorption (see Figure 1(c)) and is used for correcting fluxes of PAHs and lines, is also presented. We find the obscuration in the ring to be moderate, ranging from $\tau_{9.7} = 0.4\text{--}1.0$ when assuming a mixed geometry. To demonstrate the variation of the PAH profiles in the ring, Figures 2(b)–(d) show the zoomed-in views of the continuum-subtracted spectra that include the main PAH features at 6.2 , 7.7 , and $11.3\ \mu\text{m}$. The regions (R1, R7, and R7b) are chosen to span the range of the PAH 6.2/7.7 space. The extinction-corrected PAH flux measurements in this analysis can be found in Table 1. The uncertainties of the derived PAH ratios are typically $\sim 5\%\text{--}10\%$ based on the *CAFE* fits, with the nucleus spectrum having relatively higher uncertainties ($\sim 15\%$) due to low PAH equivalent widths.

In Figure 3, we overlay our individual PAH ratio measurements on the theoretical tracks of average grain size and ionization taken from Draine et al. (2021a).³⁵ The spectral fits

show the PAH molecules in the ring typically consist of $\sim 150\text{--}400$ carbon atoms. The grain size and ionization state probed by the 6.2/7.7 and 11.3/7.7 PAH ratios both vary by 30% throughout the ring (R1–R11). Such variations are within the range of normal star-forming galaxies in the GOALS (Stierwalt et al. 2014), SINGS (Smith et al. 2007), and ASESS (Lai et al. 2020) surveys, and likely reflect the distribution of heating intensity in the PDRs around the ring. The inset of Figure 3 is a zoomed-in view to show the PAH variations along the radial direction in four regions (R1, R2, R7, and R10) that have inner ring extractions. The four radial tracks all show gradual decrease of the PAH 6.2/7.7 ratio toward the center, suggesting an increase in the fraction of large grains relative to small grains. However, the change of ionization probed by the PAH 11.3/7.7 ratio is not pronounced except for R7b, which shows a factor of 2 decrease. The PAH bands are exceedingly weak in the nuclear spectrum (see Figure 1(c)), which makes constraining the PAH band ratios at very low PAH equivalent widths challenging. The strong [Ne VI] emission line at $7.65\ \mu\text{m}$ does not affect the measured $7.7\ \mu\text{m}$ PAH flux, since the coronal line is extremely narrow and can be well separated from the broad PAH feature in the *CAFE* fit. The nuclear spectrum does formally have a surprisingly large 6.2/7.7 PAH band flux ratio, but given the measured uncertainty, the 6.2/7.7 ratio is not significantly different than most of the ring points. The PAH 11.3/7.7 ratio, however, is lower than most of the ring positions (see Figure 3).

Investigating the relationship between the PAH ratios and [Ne III]/[Ne II], which is an indicator of the hardness of the local radiation field, can shed light on the mechanism that changes the grain size population. In Figure 4(a), we find a downward trend between the ratio of PAH 6.2/7.7 and [Ne III]/[Ne II]. All six regions that probe the inner edge of the ring (R1a, R2a/b, R7a/b, and R10a) show low PAH 6.2/7.7 ratios with increasing [Ne III]/[Ne II] as the regions are closer to the nucleus. No obvious correlation is found between 11.3/7.7 and [Ne III]/[Ne II].

Even though the main part of the ring is clearly separated from the central source by about $1''.5$, the radiation hardness measured in the ring and traced by [Ne III]/[Ne II] may be contaminated by the asymmetric and extended features of the PSF from the bright central source. Thus, separating optical artifacts from real variations in the local radiation hardness is critical for studying the effects on the small grains in the ring. A few standard stars have been observed by the JWST program 1050 (PI: Vandenbussche) for the purpose of MIRI MRS photometric calibration. We use one of the standard stars, HD 159222, as a reference and scale the neon line fluxes estimated in the nucleus (Armus et al. 2022) according to the locations of the extracted regions to estimate the contaminant level. We find the PSF from the AGN has only limited impact on the measured [Ne III]/[Ne II] ratio, which can be enhanced, at most, by about 5% at the locations of our extracted spectra.

3.2. H_2 Rotational Lines

H_2 transitions are bright in the mid-infrared spectra in star-forming regions and arise through thermal processes such that collisions maintain the lowest rotational levels of H_2 ($\nu = 0$). We measure pure rotational H_2 lines from S(1)–S(7) in each spectrum using a local continuum fit and correct for the extinction using the opacity given by *CAFE* (see Table 2 for extinction-corrected H_2 flux measurements). Even though there are issues with the $\sim 17\ \mu\text{m}$ regime of the preliminary MIRI

³⁵ Data are obtained from Draine et al. (2021b). The tracks are generated by assuming the Bruzual & Charlot (2003) interstellar radiation field with a radiation strength parameter $\log U = 2$.

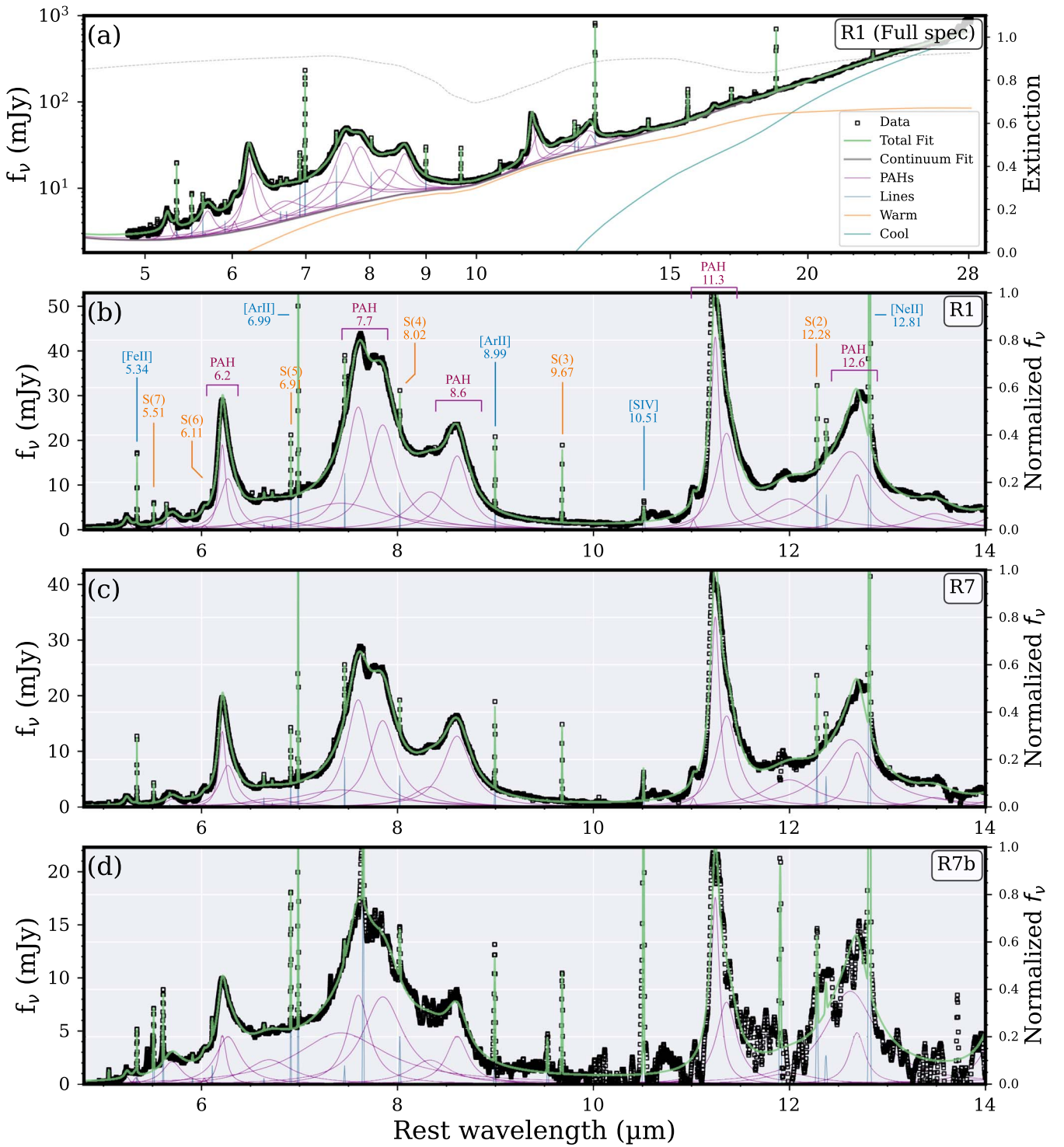


Figure 2. (a) R1 Spectrum with the full JWST MIRI MRS coverage from 5 to 28 μm . The dashed line indicates the extinction curve used in the CAFE decomposition. The data are shown in black, and the green line represents the total fit. The gray line shows the underlying continuum made of the cool dust (cyan), warm dust (orange), and hot dust component (not shown). The purple lines sitting above the continuum are the polycyclic aromatic hydrocarbon (PAH) features, while the blue lines are the atomic and molecular spectral lines. (b)–(d) The zoomed-in view of the R1, R7, and R7b continuum-subtracted spectra with key diagnostics and their corresponding wavelengths labeled. These three spectra cover the range of PAH variation in this study and are plotted to the peak of 11.3 μm PAH to ease the comparison between different PAH ratios.

MRS commissioning wavelength solution that can introduce spurious line splitting³⁶, the S(1) line fluxes are not significantly affected. The seven detected H_2 lines allow us to perform a temperature distribution power-law fit as introduced

³⁶ The issues are resolved in more recent versions.

by Togi & Smith (2016) and estimate molecular gas mass in each region. The power-law index reflects the temperature distribution of the gas—a smaller value indicates relatively high warm gas mass fraction. The power-law indices in the ring (R1–R11) range from 4.9 to 5.3, with an average value of 5.1 ± 0.1 , comparable to that found for the SINGS galaxies

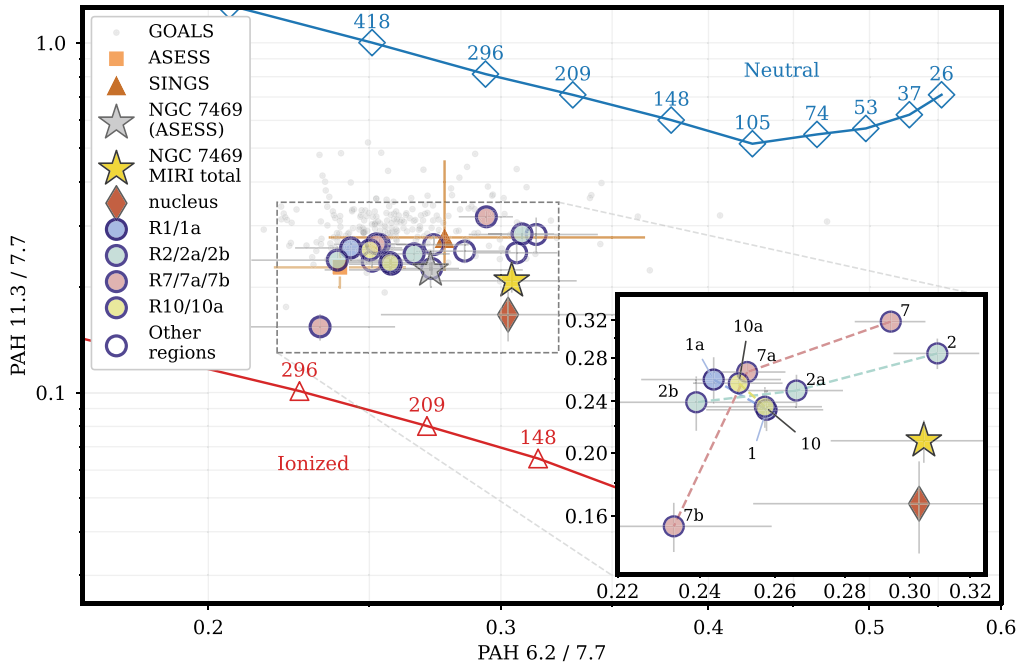


Figure 3. The interband ratios of the three main polycyclic aromatic hydrocarbon (PAH) bands at 6.2, 7.7, and 11.3 μm in the 17 regions extracted from the star-forming ring. The two tracks indicate the theoretical values for neutral and ionized PAHs with corresponding numbers of carbon atoms from Draine et al. (2021a). The star symbol indicates the PAH ratios derived from the total extraction of NGC 7469 in the MIRI MRS (Armus et al. 2022), while the red diamond is the ratio derived from the central nucleus. For comparison, the galaxies in GOALS (Stierwalt et al. 2014) are shown in gray points, along with points showing the 20%–80% range in star-forming galaxies from surveys of ALESS (Lai et al. 2020) and SINGS (Smith et al. 2007). The gray star indicates the measurement of the combined AKARI +Spitzer spectrum of NGC 7469 in ALESS. (inset) The zoom-in of the regions used for radial variation studies. Regions with *a* and *b* designations are those close to the nucleus as shown in Figure 1 (b). Every region in the inset shows a trend of decreasing PAH 6.2/7.7 ratio when progressively moving toward the center, suggesting an increase of the grain size distribution.

Table 1
PAH Band and Emission Line Fluxes

Regions	R.A. (ICRS)	Decl. (ICRS)	PAH 6.2 μm	PAH 7.7 μm ($\times 10^{-16} \text{ W m}^{-2}$)	PAH 11.3 μm	[Ne II] 12.81 μm ($\times 10^{-17} \text{ W m}^{-2}$)	[Ne III] 15.56 μm
R1	23:03:15.5147	+8:52:25.111	5.31 ± 0.19	20.61 ± 1.04	4.80 ± 0.25	12.07 ± 0.16	1.14 ± 0.03
R2	23:03:15.5791	+8:52:24.734	4.72 ± 0.10	15.29 ± 0.61	4.34 ± 0.16	17.16 ± 0.13	1.28 ± 0.02
R3	23:03:15.6279	+8:52:25.076	3.64 ± 0.11	12.78 ± 0.74	3.24 ± 0.16	7.41 ± 0.08	1.44 ± 0.02
R4	23:03:15.7021	+8:52:25.267	3.65 ± 0.18	11.58 ± 0.86	3.28 ± 0.30	8.06 ± 0.06	1.03 ± 0.02
R5	23:03:15.6789	+8:52:25.999	4.04 ± 0.09	16.12 ± 0.58	3.83 ± 0.09	8.17 ± 0.07	2.54 ± 0.03
R6	23:03:15.7192	+8:52:26.531	3.36 ± 0.12	13.24 ± 0.64	3.51 ± 0.20	6.62 ± 0.05	0.95 ± 0.02
R7	23:03:15.6853	+8:52:27.197	3.71 ± 0.07	12.63 ± 0.40	4.02 ± 0.08	11.24 ± 0.07	1.14 ± 0.02
R8	23:03:15.6422	+8:52:27.714	3.29 ± 0.10	10.72 ± 0.52	2.69 ± 0.12	5.95 ± 0.04	0.68 ± 0.01
R9	23:03:15.5919	+8:52:27.380	4.35 ± 0.08	15.98 ± 0.53	3.61 ± 0.10	8.67 ± 0.07	1.30 ± 0.02
R10	23:03:15.5482	+8:52:26.884	3.54 ± 0.10	13.75 ± 0.76	3.24 ± 0.15	8.27 ± 0.07	1.29 ± 0.02
R11	23:03:15.5096	+8:52:26.217	3.74 ± 0.10	13.68 ± 0.57	3.62 ± 0.18	8.92 ± 0.06	1.02 ± 0.01
R1a	23:03:15.5366	+8:52:25.419	6.37 ± 0.27	26.14 ± 1.58	6.77 ± 0.38	13.43 ± 0.18	2.55 ± 0.05
R2a	23:03:15.5881	+8:52:25.210	6.18 ± 0.16	23.24 ± 1.02	5.79 ± 0.21	15.72 ± 0.13	2.05 ± 0.03
R7a	23:03:15.6621	+8:52:26.797	3.68 ± 0.08	14.57 ± 0.53	3.88 ± 0.07	10.06 ± 0.08	2.53 ± 0.03
R10a	23:03:15.5728	+8:52:26.578	2.22 ± 0.07	8.87 ± 0.31	2.27 ± 0.02	6.38 ± 0.08	2.83 ± 0.06
R2b	23:03:15.6011	+8:52:25.619	6.16 ± 0.40	25.75 ± 2.36	6.16 ± 0.18	13.19 ± 0.18	7.50 ± 0.12
R7b	23:03:15.6401	+8:52:26.555	2.24 ± 0.17	9.60 ± 0.76	1.48 ± 0.05	5.10 ± 0.08	5.48 ± 0.08
Nucleus	23:03:15.6155	+8:52:26.180	1.59 ± 0.26	5.24 ± 0.31	0.87 ± 0.14	7.63 ± 0.28	12.19 ± 0.27

(4.8 ± 0.6 ; Togi & Smith 2016). We estimate the warm H_2 gas (no heavy element correction) with a temperature above 200 K to be $(1.2 \pm 0.3) \times 10^7 M_\odot$ in the ring. Extrapolating to 50 K, the total H_2 gas mass in the ring is $(1.8 \pm 0.4) \times 10^9 M_\odot$, which agrees to our measured H_2 mass of $(1.6 \pm 0.3) \times 10^9 M_\odot$ derived from the ALMA CO(1-0) map (PI: T. Izumi) assuming the Galactic X_{CO} conversion factor.

In Figure 4(b), a correlation between the [Ne III]/[Ne II] ratio and H_2/PAH is presented. Regions with a locally harder

radiation field have more warm molecular gas in relation to the PAH emission. Typically, for low-luminosity star-forming galaxies, the ratio of H_2/PAH remains within a range of a factor of 3 over ~ 3 orders of magnitude in $L(\text{H}_2)$ (Roussel et al. 2007). In contrast, AGNs show an order of magnitude higher H_2/PAH ratios due to the enhancement of the H_2 emission heated by shocks and X-rays. The H_2/PAH ratio therefore can be used to identify regions heated by shocks or excess UV/X-ray radiation above and beyond that emitted by young stars in

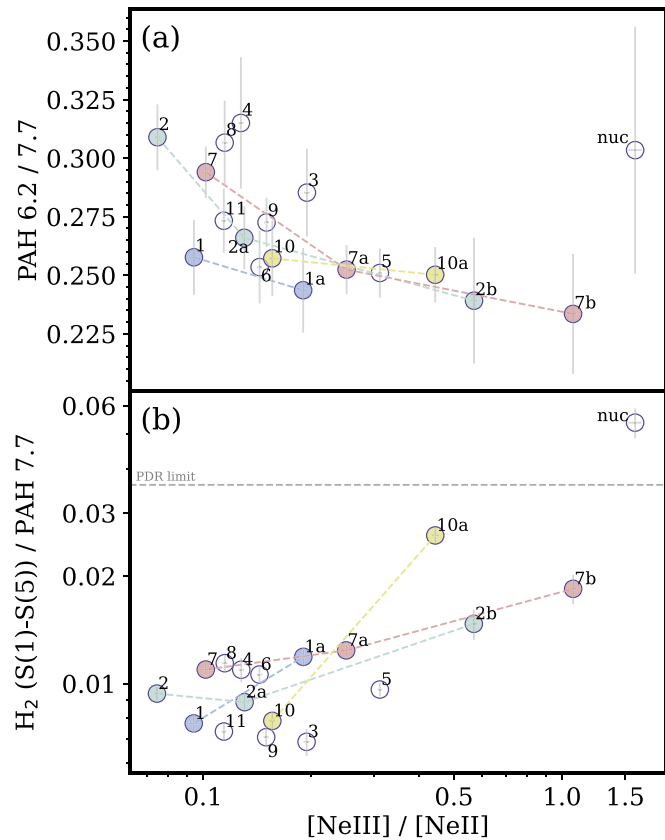


Figure 4. (a) The correlation between polycyclic aromatic hydrocarbon (PAH) sizes, as indicated by the 6.2/7.7 PAH ratio, and hardness of the radiation fields. Collectively, PAH 6.2/7.7 shows a slight downward trend, suggesting smaller grains are likely being destroyed as the hardness of the radiation field increases. This effect is more pronounced when compared to points along the same radial direction (linked by dashed lines) with different distances to the nucleus. The nuclear point does not appear to follow this downward trend but it has a relatively large uncertainty. (b) H_2 -to-PAH ratio shows an increasing trend with increasing $[Ne III]/[Ne II]$. Here the H_2 flux represents the sum of the low rotational lines S(1)–S(5), while PAH represents the flux from the 7.7 μm PAH. We find that H_2/PAH in the ring are well within the range of normal PDR models (Guillard et al. 2012), suggesting the H_2 gas is predominantly heated by young stars. For comparison, the nucleus lies well above the PDR limit, indicative of either AGN heating or shocks in the vicinity of the AGN.

PDRs. In the case of NGC 7469 in particular, we can test whether the wind or the radiation from the Seyfert 1.5 nucleus is significantly heating the molecular gas in the starburst ring. To measure the H_2/PAH ratio throughout the ring, we use the sum of H_2 S(1)–S(5) to represent $L(H_2)$ and the PAH band at 7.7 μm to represent PAH luminosity. In Guillard et al. (2012), the authors suggested the ratio of the PDR limit of S(0)–S(3)/PAH 7.7 = 0.04; only ratios above this threshold can be ascribed to shock heated H_2 . To better compare with this PDR model, we use the averaged S(0)–S(3) to S(1)–S(5) ratio taken from the PDR modeling results in Habart et al. (2011) to make the translation. We find the ratio of the combined fluxes S(1)–S(5)/S(0)–S(3) to be ~ 0.9 . Hence, the H_2/PAH ratios throughout the ring are well within the PDR range (0.036), suggesting that young, massive stars are likely the dominant heating source of the warm molecular gas. The variation in the H_2/PAH ratio may reflect differences in the age of the population and/or the proximity of the young stars to their natal molecular clouds. The AGN spectrum, however, shows an elevated H_2/PAH ratio lying above the PDR limit.

3.3. Star Formation Rate in the Ring

The SFR in the ring of NGC 7469 can be estimated with the Pf α , [Ne II], and [Ne III] measurements. By assuming a case B scenario ($n_e = 10,000 \text{ cm}^{-3}$, $T_e = 10,000 \text{ K}$; Hummer & Storey 1987), we translate our Pf α flux to $H\alpha$ and apply Equation (2) in Murphy et al. (2011) to derive the SFR in our extracted regions. The estimated $SFR_{Pf\alpha}$ in each extracted region ranges from 0.3 to $1 M_\odot \text{ yr}^{-1}$. An alternative way to estimate the SFR is by using the neon lines (Ho & Keto 2007; Zhuang et al. 2019). Applying Equation (13) in Ho & Keto (2007), we find the estimated SFR_{Ne} in the extracted region ranges from 1 to $3 M_\odot \text{ yr}^{-1}$, a factor of 3 higher than the range inferred from the recombination line. Therefore, we find the SFR in the ring to range from 10 to $30 M_\odot \text{ yr}^{-1}$ when integrating over R1–R11, which agrees well with the SFR of $20 M_\odot \text{ yr}^{-1}$ estimated using the 33 GHz ratio continuum from Song et al. (2021).

4. Discussion

The results presented in Sections 3.1 and 3.2 paint a consistent picture of the central AGN having a measurable, yet moderate impact on the dust and gas properties throughout most of the starburst ring. Changes are most evident as one moves off the bright star-forming regions in the ring toward the nucleus. In Figures 1(c) and 3, we show that the PAHs are clearly fainter with respect to the continuum in regions closer to the AGN (see also Armus et al. 2022), and the 6.2/7.7 PAH flux ratio is lower at the inner edge of the ring. The lack of a pronounced increase in the 11.3/7.7 flux ratio in the nucleus is somewhat surprising, given a number of Spitzer/IRS results (Smith et al. 2007; Diamond-Stanic & Rieke 2010) that show 11.3/7.7 ratios of nearly unity or above in some nearby Seyfert galaxies. This discrepancy may be due to the large difference between the physical scales probed by JWST and Spitzer, with Spitzer being unable to cleanly separate the influences of bright stellar bulges (hence starlight heating) from the effects of the AGN. It may also simply reflect the range in properties of the dusty ISM in Seyfert galaxies with and without circumnuclear starbursts and prominent stellar bulges. The fact that there is a trend of decreasing 6.2/7.7 PAH flux ratio with increasing $[Ne III]/[Ne II]$ ratio suggests that the AGN has an effect on the average grain size on the inner edge of the ring, but the magnitude of this effect in the MIRI/MRS data is comparable to that seen in the star-forming regions themselves.

A similar picture emerges when looking at the warm molecular gas in the NGC 7469 ring. There is no clear sign of shocks from the outflowing wind heating the molecular gas, as the H_2 -to-PAH ratios are within the PDR limit (Figure 4(b)) and agree well with the ratios reported in the H II nuclei in Roussel et al. (2007). The atomic fine structure line flux ratios, in particular those of neon and sulfur (e.g., Inami et al. 2013), are also inconsistent with shock heating of the gas in the ring. Together with the fact that we see no azimuthal correlation with the direction of the outflow mapped in coronal lines by Müller-Sánchez et al. (2011) suggests a minimal impact of the outflow on the star-forming gas in the ring. Some shocked gas may be present near region R10a, which has the highest H_2 -to-PAH ratio, consistent with a region of increased velocity dispersion seen by U et al. (2022). In addition, the nuclear spectrum shows an elevated H_2 -to-PAH ratio suggestive of either AGN heating or shocks in the vicinity of the nucleus. Other more powerful AGNs (e.g., some low redshift radio galaxies) show evidence

Table 2
H₂ Line Fluxes

Regions	S(1) 17.04 μm	S(2) 12.28 μm	S(3) 9.67 μm	S(4) 8.03 μm	S(5) 6.91 μm	S(6) 6.11 μm	S(7) 5.51 μm
R1	4.70 \pm 0.33	2.55 \pm 0.08	3.95 \pm 0.17	1.65 \pm 0.13	3.08 \pm 0.10	0.50 \pm 0.07	1.34 \pm 0.05
R2	4.63 \pm 0.15	2.38 \pm 0.09	3.43 \pm 0.10	1.35 \pm 0.09	2.55 \pm 0.08	0.36 \pm 0.10	0.98 \pm 0.07
R3	1.83 \pm 0.53	1.80 \pm 0.07	2.48 \pm 0.11	0.97 \pm 0.07	1.71 \pm 0.08	0.33 \pm 0.05	0.59 \pm 0.06
R4	4.29 \pm 0.22	2.17 \pm 0.07	3.20 \pm 0.09	1.04 \pm 0.06	1.98 \pm 0.07	0.40 \pm 0.03	0.82 \pm 0.06
R5	4.31 \pm 0.30	2.52 \pm 0.12	3.95 \pm 0.15	1.71 \pm 0.09	3.00 \pm 0.12	0.55 \pm 0.10	1.27 \pm 0.08
R6	4.80 \pm 0.12	2.41 \pm 0.09	3.28 \pm 0.09	1.26 \pm 0.06	2.24 \pm 0.12	0.36 \pm 0.06	0.88 \pm 0.15
R7	4.08 \pm 0.20	2.25 \pm 0.06	3.64 \pm 0.08	1.36 \pm 0.06	2.46 \pm 0.09	0.45 \pm 0.05	1.24 \pm 0.13
R8	3.76 \pm 0.07	1.91 \pm 0.06	3.25 \pm 0.10	1.19 \pm 0.06	2.09 \pm 0.07	0.37 \pm 0.10	0.91 \pm 0.06
R9	1.79 \pm 0.58	2.20 \pm 0.06	3.36 \pm 0.19	1.49 \pm 0.07	2.48 \pm 0.09	0.43 \pm 0.05	1.12 \pm 0.07
R10	3.31 \pm 0.29	1.78 \pm 0.07	2.73 \pm 0.12	1.09 \pm 0.06	1.86 \pm 0.07	0.28 \pm 0.05	0.88 \pm 0.08
R11	3.31 \pm 0.13	1.69 \pm 0.07	2.48 \pm 0.14	0.96 \pm 0.06	1.62 \pm 0.08	0.31 \pm 0.06	0.61 \pm 0.07
R1a	9.74 \pm 0.36	4.82 \pm 0.14	7.81 \pm 0.19	3.28 \pm 0.14	5.36 \pm 0.13	1.05 \pm 0.12	2.55 \pm 0.14
R2a	6.19 \pm 0.24	3.14 \pm 0.12	5.16 \pm 0.20	2.34 \pm 0.10	3.75 \pm 0.13	0.52 \pm 0.13	1.75 \pm 0.11
R7a	4.44 \pm 0.19	2.88 \pm 0.08	4.86 \pm 0.13	2.07 \pm 0.09	3.83 \pm 0.09	0.63 \pm 0.05	1.73 \pm 0.11
R10a	3.56 \pm 0.48	3.29 \pm 0.20	6.94 \pm 0.36	3.24 \pm 0.22	6.00 \pm 0.22	1.16 \pm 0.12	2.97 \pm 0.10
R2b	4.15 \pm 0.76	4.76 \pm 0.55	10.11 \pm 0.53	6.36 \pm 0.46	12.44 \pm 0.37	2.53 \pm 0.21	6.80 \pm 0.51
R7b	3.38 \pm 0.71	2.20 \pm 0.30	3.83 \pm 0.25	2.61 \pm 0.33	5.66 \pm 0.07	1.14 \pm 0.06	3.07 \pm 0.57
Nucleus	3.79 \pm 1.45	2.77 \pm 1.29	6.01 \pm 0.59	4.70 \pm 0.52	10.89 \pm 0.21	2.24 \pm 0.14	6.22 \pm 1.92

Note. All H₂ pure rotational line fluxes are in units of 10^{-18} W m⁻².

for abundant shocked, warm molecular gas in their mid-infrared spectra, implying strong feedback on the dense ISM (e.g., Ogle et al. 2007). More MIRI and NIRSPEC integral-field unit observations of nearby AGNs spanning a wide range in power and orientation are clearly needed to reveal general trends of the effects of feedback on the dust and molecular gas on sub-kiloparsec scales.

5. Summary

In this Letter, we present JWST observations using MIRI MRS of the dust and gas in the circumnuclear star-forming ring in the nearby Seyfert galaxy NGC 7469 on ~ 100 pc scales. We find:

1. The PAH surface brightness varies by a factor of 3 throughout the ring, with the the brightest emission to the southwest and northeast. The interband PAH flux ratios of 6.2/7.7 and 11.3/7.7, span a range comparable to that of nearby star-forming galaxies, with variations of $\sim 30\%$ suggestive of relatively small variations in the average size and ionization state of the small grains. The largest change in the PAH band ratios occurs at the inner edge of the ring, moving toward the central AGN where the grains appear to increase in size and become more ionized. The PAH emission is significantly reduced in the region around the nucleus. There is no indication of a more neutral grain population in the central 100 pc.
2. A suite of H₂ pure rotational lines are detected throughout the ring. The H₂ flux ratios translate to the mass of warm molecular gas of $1.2 \times 10^7 M_{\odot}$ at a temperature higher than 200 K and a total molecular mass of $1.8 \times 10^9 M_{\odot}$ when extrapolating down to 50 K. Although the H₂/PAH ratios do correlate with the ionization of the ionized gas as measured by the [Ne III]/[Ne II] ratio, possibly indicating some heating by the AGN, the H₂/PAH ratios in the ring are well within the range of normal PDRs. The nuclear spectrum, however, does show an elevated H₂/PAH ratio, indicative of AGN heating or the presence

of shocks. Taken together, our results suggest the presence of feedback from the AGN on the inner part of the ring and central ISM, but minimal impact of shocks and hard ionizing photons on the star-forming gas throughout most of the ring.

Our study demonstrates that with JWST the resolved properties of the near nuclear ISM can be finally studied in detail, in even the dustiest galaxies, on the scales of individual star-forming regions. Future observations with JWST will undoubtedly shed great light on the importance of feedback from AGNs on star formation in galaxies, using the powerful dust and gas tracers of the multiphase ISM available in the mid-infrared.











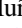


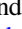




This work is based on observations made with the NASA/ESA/CSA JWST. T.S.-Y.L. acknowledges funding support from NASA grant JWST-ERS-01328. The data were obtained from the Mikulski Archive for Space Telescopes at the Space Telescope Science Institute, which is operated by the Association of Universities for Research in Astronomy, Inc., under NASA contract NAS 5-03127 for JWST. These observations are associated with program #1328 and can be accessed via doi:[10.17909/0fe2-cf33](https://doi.org/10.17909/0fe2-cf33). V.U. acknowledges funding support from NASA Astrophysics Data Analysis Program (ADAP) grant 80NSSC20K0450. The Flatiron Institute is supported by the Simons Foundation. H.I. and T.B. acknowledge support from JSPS KAKENHI grant No. JP21H01129 and the Ito Foundation for Promotion of Science. A.M.M. acknowledges support from the National Science Foundation under grant No. 2009416. A.S.E. and S.L. acknowledge support from NASA grant HST-GO15472 and HST-GO16914. Y.S. was funded in part by the NSF through the Grote Reer Fellowship Program administered by Associated Universities, Inc./National Radio Astronomy Observatory. S.A. gratefully acknowledges support from an ERC Advanced grant 789410, from the Swedish Research Council and from the Knut and Alice Wallenberg (KAW) Foundation. F.K. acknowledges support from the Spanish program Unidad de Excelencia María de Maeztu

CEX2020-001058-M, financed by MCIN/AEI/10.13039/501100011033. K.I. acknowledges support by the Spanish MCIN under grant PID2019-105510GB-C33/AEI/10.13039/501100011033. F.M-S. acknowledges support from NASA through ADAP award 80NSSC19K1096. Finally, this research has made use of the NASA/IPAC Extragalactic Database (NED), which is operated by the Jet Propulsion Laboratory, California Institute of Technology, under contract with the National Aeronautics and Space Administration.

Facilities: JWST (MIRI), MAST, NED.

Software: Astropy (Astropy Collaboration et al. 2013, 2018), CAFE (Marshall et al. 2007), JWST Science Calibration Pipeline (Bushouse et al. 2022), Imfit (Newville et al. 2014), Matplotlib (Hunter 2007), Numpy (van der Walt et al. 2011), QFitsView (Ott 2012), SciPy (Virtanen et al. 2020).

ORCID iDs

Thomas S.-Y. Lai (賴劭愉)  <https://orcid.org/0000-0001-8490-6632>
 Lee Armus  <https://orcid.org/0000-0003-3498-2973>
 Vivian U  <https://orcid.org/0000-0002-1912-0024>
 Tanio Díaz-Santos  <https://orcid.org/0000-0003-0699-6083>
 Kirsten L. Larson  <https://orcid.org/0000-0003-3917-6460>
 Aaron Evans  <https://orcid.org/0000-0003-2638-1334>
 Matthew A. Malkan  <https://orcid.org/0000-0001-6919-1237>
 Philip Appleton  <https://orcid.org/0000-0002-7607-8766>
 Jeff Rich  <https://orcid.org/0000-0002-5807-5078>
 Hanae Inami  <https://orcid.org/0000-0003-4268-0393>
 Thomas Bohn  <https://orcid.org/0000-0002-4375-254X>
 Jed McKinney  <https://orcid.org/0000-0002-6149-8178>
 Luke Finnerty  <https://orcid.org/0000-0002-1392-0768>
 David R. Law  <https://orcid.org/0000-0002-9402-186X>
 Sean T. Linden  <https://orcid.org/0000-0002-1000-6081>
 Anne M. Medling  <https://orcid.org/0000-0001-7421-2944>
 George C. Privon  <https://orcid.org/0000-0003-3474-1125>
 Yiqing Song  <https://orcid.org/0000-0002-3139-3041>
 Sabrina Stierwalt  <https://orcid.org/0000-0002-2596-8531>
 Paul P. van der Werf  <https://orcid.org/0000-0001-5434-5942>
 Loreto Barcos-Muñoz  <https://orcid.org/0000-0003-0057-8892>
 J. D. T. Smith  <https://orcid.org/0000-0003-1545-5078>
 Aditya Togi  <https://orcid.org/0000-0001-5042-3421>
 Susanne Aalto  <https://orcid.org/0000-0002-5828-7660>
 Torsten Böker  <https://orcid.org/0000-0002-5666-7782>
 Vassilis Charmandaris  <https://orcid.org/0000-0002-2688-1956>
 Justin Howell  <https://orcid.org/0000-0001-6028-8059>
 Kazushi Iwasawa  <https://orcid.org/0000-0002-4923-3281>
 Francisca Kemper  <https://orcid.org/0000-0003-2743-8240>
 Joseph M. Mazzarella  <https://orcid.org/0000-0002-8204-8619>
 Eric J. Murphy  <https://orcid.org/0000-0001-7089-7325>
 Michael J. I. Brown  <https://orcid.org/0000-0002-1207-9137>
 Christopher C. Hayward  <https://orcid.org/0000-0003-4073-3236>
 Jason Marshall  <https://orcid.org/0000-0001-7712-8465>
 David Sanders  <https://orcid.org/0000-0002-1233-9998>
 Jason Surace  <https://orcid.org/0000-0001-7291-0087>

References

- Alexander, D. M., & Hickox, R. C. 2012, *NewAR*, 56, 93
 Alonso-Herrero, A., Pereira-Santaella, M., Rieke, G. H., & Rigopoulou, D. 2012, *ApJ*, 744, 2
 Armus, L., Charmandaris, V., Bernard-Salas, J., et al. 2007, *ApJ*, 656, 148
 Armus, L., Charmandaris, V., & Soifer, B. T. 2020, *NatAs*, 4, 467
 Armus, L., Charmandaris, V., Spoon, H. W. W., et al. 2004, *ApJS*, 154, 178
 Armus, L., Lai, T., U, V., et al. 2022, arXiv:2209.13125
 Asmus, D., Gandhi, P., Hönig, S. F., Smette, A., & Duschl, W. J. 2015, *MNRAS*, 454, 766
 Astropy Collaboration, Price-Whelan, A. M., Sipőcz, B. M., et al. 2018, *AJ*, 156, 123
 Astropy Collaboration, Robitaille, T. P., Tollerud, E. J., et al. 2013, *A&A*, 558, A33
 Bohn, T., Inami, H., Diaz-Santos, T., et al. 2022, arXiv:2209.04466
 Bruzual, G., & Charlot, S. 2003, *MNRAS*, 344, 1000
 Bushouse, H., Eisenhamer, J., Dencheva, N., et al. 2022, spacetelescope/jwst: JWST, v1.6.2, Zenodo, doi:10.5281/zenodo.6984366
 Diamond-Stanic, A. M., & Rieke, G. H. 2010, *ApJ*, 724, 140
 Díaz-Santos, T., Alonso-Herrero, A., Colina, L., Ryder, S. D., & Knapen, J. H. 2007, *ApJ*, 661, 149
 Díaz-Santos, T., Armus, L., Charmandaris, V., et al. 2017, *ApJ*, 846, 32
 Draine, B. T., Li, A., Hensley, B. S., et al. 2021a, *ApJ*, 917, 3
 Draine, B. T., Li, A., Hensley, B. S., et al. 2021b, PAH emission: Dependence on Starlight Spectrum, Intensity, PAH Size Distribution, and PAH Ionization, v1, Harvard Dataverse, doi:10.7910/DVN/LPUHIQ
 Guillard, P., Ogle, P. M., Emonts, B. H. C., et al. 2012, *ApJ*, 747, 95
 Habart, E., Abergel, A., Boulanger, F., et al. 2011, *A&A*, 527, A122
 Hao, L., Wu, Y., Charmandaris, V., et al. 2009, *ApJ*, 704, 1159
 Ho, L. C., & Keto, E. 2007, *ApJ*, 658, 314
 Howell, J. H., Mazzarella, J. M., Chan, B. H. P., et al. 2007, *AJ*, 134, 2086
 Hummer, D. G., & Storey, P. J. 1987, *MNRAS*, 224, 801
 Hunter, J. D. 2007, *CSE*, 9, 90
 Inami, H., Armus, L., Charmandaris, V., et al. 2013, *ApJ*, 777, 156
 Izumi, T., Nguyen, D. D., Imanishi, M., et al. 2020, *ApJ*, 898, 75
 Jensen, J. J., Hönig, S. F., Rakshit, S., et al. 2017, *MNRAS*, 470, 3071
 Labiano, A., Argyriou, I., Álvarez-Márquez, J., et al. 2021, *A&A*, 656, A57
 Lai, T.-S.-Y., Smith, J. D. T., Baba, S., Spoon, H. W. W., & Imanishi, M. 2020, *ApJ*, 905, 55
 Landt, H., Bentz, M. C., Ward, M. J., et al. 2008, *ApJS*, 174, 282
 Le Floc'h, E., Papovich, C., Dole, H., et al. 2005, *ApJ*, 632, 169
 Lu, K.-X., Wang, J.-G., Zhang, Z.-X., et al. 2021, *ApJ*, 918, 50
 Magorrian, J., Tremaine, S., Richstone, D., et al. 1998, *AJ*, 115, 2285
 Marshall, J. A., Elitzur, M., Armus, L., Diaz-Santos, T., & Charmandaris, V. 2018, *ApJ*, 858, 59
 Marshall, J. A., Herter, T. L., Armus, L., et al. 2007, *ApJ*, 670, 129
 Müller-Sánchez, F., Prieto, M. A., Hicks, E. K. S., et al. 2011, *ApJ*, 739, 69
 Murphy, E. J., Condon, J. J., Schinnerer, E., et al. 2011, *ApJ*, 737, 67
 Newville, M., Stensitzki, T., Allen, D. B., & Ingargiola, A. 2014, LMFIT: Non-Linear Least-Square Minimization and Curve-Fitting for Python, v0.8.0, Zenodo, doi:10.5281/zenodo.11813
 Nguyen, D. D., Izumi, T., Thater, S., et al. 2021, *MNRAS*, 504, 4123
 O'Dowd, M. J., Schiminovich, D., Johnson, B. D., et al. 2009, *ApJ*, 705, 885
 Ogle, P., Antonucci, R., Appleton, P. N., & Whyson, D. 2007, *ApJ*, 668, 699
 Oschmann, J. M., Clampin, M., Fazio, G. G., et al. 2014, *Proc. SPIE*, 9143, 91433X
 Ott, T. 2012, QFitsView: FITS file viewer, Astrophysics Source Code Library, ascl:1210.019
 Peeters, E., Spoon, H. W. W., & Tielens, A. G. G. M. 2004, *ApJ*, 613, 986
 Peterson, B. M., Grier, C. J., Home, K., et al. 2014, *ApJ*, 795, 149
 Petric, A. O., Armus, L., Howell, J., et al. 2011, *ApJ*, 730, 28
 Rieke, G. H., Wright, G. S., Böker, T., et al. 2015, *PASP*, 127, 584
 Robledo-Orús, A. C., Torres-Papaqui, J. P., Longinotti, A. L., et al. 2021, *ApJL*, 906, L6
 Roussel, H., Helou, G., Hollenbach, D. J., et al. 2007, *ApJ*, 669, 959
 Sajina, A., Lacy, M., & Pope, A. 2022, *Univ*, 8, 356
 Smith, J. D. T., Draine, B. T., Dale, D. A., et al. 2007, *ApJ*, 656, 770
 Song, Y., Linden, S. T., Evans, A. S., et al. 2021, *ApJ*, 916, 73
 Stierwalt, S., Armus, L., Charmandaris, V., et al. 2014, *ApJ*, 790, 124
 Tielens, A. G. G. M. 2008, *ARA&A*, 46, 289
 Togi, A., & Smith, J. D. T. 2016, *ApJ*, 830, 18
 U, V. 2022, *Univ*, 8, 392
 U, V., Lai, T., Bianchin, M., et al. 2022, *ApJL*, 940, L5
 van der Walt, S., Colbert, S. C., & Varoquaux, G. 2011, *CSE*, 13, 22
 Veilleux, S., Rupke, D. S. N., Kim, D.-C., et al. 2009, *ApJS*, 182, 628
 Verstraete, L., Pech, C., Moutou, C., et al. 2001, *A&A*, 372, 981
 Virtanen, P., Gommers, R., Oliphant, T. E., et al. 2020, *NatMe*, 17, 261
 Wells, M., Pel, J.-W., Glasse, A., et al. 2015, *PASP*, 127, 646
 Wu, Y., Charmandaris, V., Hao, L., et al. 2006, *ApJ*, 639, 157
 Xu, X., & Wang, J. 2022, *ApJ*, 933, 110
 Zhuang, M.-Y., Ho, L. C., & Shanguan, J. 2019, *ApJ*, 873, 103